

Current as of March 13, 2015

High-order terms in the renormalized perturbation theory for the Anderson impurity model

Vassilis Pandis, Alex C. Hewson

Department of Mathematics, Imperial College London, London SW7 2AZ, United Kingdom

(Dated: March 13, 2015)

We study the renormalized perturbation theory of the single-impurity Anderson model, particularly the high-order terms in the expansion of the self-energy in powers of the renormalized coupling \tilde{U} . Though the presence of counter-terms in the renormalized theory may appear to complicate the diagrammatics, we show how these can be seamlessly accommodated by carrying out the calculation order-by-order in terms of skeleton diagrams. We describe how the diagrams pertinent to the renormalized self-energy and four-vertex can be automatically generated, translated into integrals and numerically integrated. To maximize the efficiency of our approach we introduce a generalized k -particle/hole propagator, which is used to analytically simplify the resultant integrals and reduce the dimensionality of the integration. We present results for the self-energy and spectral density to fifth order in \tilde{U} , for various values of the model asymmetry, and compare them to a Numerical Renormalization Group calculation.

I. INTRODUCTION

The Anderson Impurity Model (AIM)¹ was introduced in 1961 to explain the existence of localized magnetic moments in metals with magnetic impurities. It stands today as one of the best understood impurity models, having been intensely studied by a number of methods such as the bare perturbation theory²⁻⁶, $1/N$ expansions⁷ (where N denotes the impurity orbital degeneracy), the Bethe Ansatz^{8,9} and the Numerical Renormalization Group (NRG)^{10,11} (among many others; see Ref.¹² for a review). Each of these is particularly useful in different scenarios: the bare perturbation theory excels at weak-coupling, $1/N$ expansions are asymptotically correct for highly degenerate models, the Bethe Ansatz yields exact results, but only for static quantities, and the NRG approach cannot efficiently deal with large degeneracies. Together, these methods paint a consistent picture for the physics of the model, but their abundance highlights the challenges posed even by relatively simple models of strongly correlated electrons. This in-depth understanding of the model has served to establish it as a testing ground for the development of new methods in many-body physics. Though the AIM is today well understood in the context of a single impurity, interest in it has been renewed in light of the Dynamical Mean-Field Theory¹³, which allows models of impurity lattices to be mapped — exactly in the limit of infinite dimensions — onto a single-impurity problem subject to a self-consistency consistency condition.

An important step in the understanding of impurity physics was the connection made by Nozières between the strong coupling fixed point of the Kondo model at low temperatures and Landau's theory of Fermi liquids¹⁴, in which the excited states of the model are interpreted in terms of quasi-particles which are weakly interacting¹⁵, even in the strong correlation regime. It was quickly recognized that the AIM is a Fermi Liquid in all parameter

regimes^{11,16} though this idea was not fully explored until very recently^{17,18}.

In light of the Fermi liquid interpretation, the Renormalized Perturbation Theory (RPT)¹⁹⁻²⁷ offers a convenient way of analysing the low-energy behaviour of the model. The usual Hamiltonian H of the AIM specifies the model in terms of the impurity level ϵ_d , the hybridization broadening Δ and the local Coulomb interaction U . In the renormalized theory these are replaced by effective parameters $\tilde{\epsilon}_d, \tilde{\Delta}, \tilde{U}$ which are used to define a renormalized Hamiltonian \tilde{H} of the same form as H and which, by definition, incorporates the low-energy one-particle interactions. The propagators in the renormalized theory describe the quasi-particle states, making explicit the one-to-one correspondence between the single-particle excitations of the non-interacting and interacting systems. The quasi-particle interactions can now be taken into account by constructing a perturbation theory in the renormalized parameters and organized in powers of \tilde{U} .

The RPT has a number of appealing features¹⁹. In the presence of a magnetic field the leading term of the renormalized expansion is of order \tilde{U} , and suffices to calculate the zero-temperature spin and charge susceptibilities exactly in all parameter regimes. In the absence of a magnetic field the leading term in the RPT is of order \tilde{U}^2 and leads to a simple exact expression for the second derivative of the imaginary part of the self-energy at zero frequency. This in turn can be used to derive an exact expression for the T^2 coefficient of the conductivity of the symmetric model in terms of the renormalized parameters.

In this paper we discuss the calculation of the renormalized self-energy using the diagrammatic RPT and show how this can be implemented on a computer completely automatically. Our presentation is structured as follows: We start by describing a simple algorithm to generate all relevant Feynman diagrams and retain only

those that contribute to the renormalized self-energy. Though at first the RPT seems to have a more complicated perturbational structure than the bare theory, owing to the presence of counter-terms, we show how these can be included into the calculation with minimal effort by setting up the calculation in terms of skeleton diagrams. As an intermediate step we introduce a simplification algorithm which dramatically reduces the computational complexity of the resultant integrals by factorising out sub-integrations that can be computed analytically. Finally, we carry out the numerical integrations and present results to order \tilde{U}^5 inclusive for the self-energy and spectral density in the strong correlation regime, for different values of the asymmetry, and compare these to results obtained using the NRG.

II. RENORMALIZED PERTURBATION THEORY

The effective Lagrangian for the Anderson model in the limit of an infinitely wide conduction electron band is²¹

$$\mathcal{L} = \sum_{\sigma=\uparrow,\downarrow} \bar{d}_\sigma(\tau) (\partial_\tau - \epsilon_{d,\sigma} + i\Delta) d_\sigma(\tau) + U n_\uparrow(\tau) n_\downarrow(\tau). \quad (1)$$

In the bare perturbation theory one attempts to solve Eq. (1) by taking the $U = 0$ (or Hartree-Fock) state as the starting point for a perturbation theory in powers of the interaction U . Though some useful information can be extracted this way in the weak correlation regime, the value of U in physically relevant systems is usually too large to be handled in this manner; this is precisely the challenge of strongly correlated physics. In particular, it has long been recognized that the low-energy excitations primarily responsible for the interesting physics of impurity models cannot be described perturbatively.

The difficulty of the bare perturbation theory can be ultimately traced to the unfortunate choice of the $U = 0$ state as the starting point for the perturbation expansion. As we increase U , virtual low-energy scattering processes will lead to the formation of quasi-particles on the impurity site which interact through a renormalized Coulomb interaction \tilde{U} , and whose relation to the original particles becomes increasingly tenuous. The RPT seeks to address this issue by using precisely these quasi-particle states as the starting point for the perturbation expansion in powers of the renormalized coupling. This is accomplished by writing the Lagrangian in Eq. (1) as a sum of a renormalized quasi-particle Lagrangian, which describes the quasi-particles, a renormalized interaction term and a remainder term, the *counter-term*

Lagrangian, i.e. $\mathcal{L} = \tilde{\mathcal{L}}_0 + \tilde{\mathcal{L}}_U + \mathcal{L}_{ct}$, where

$$\tilde{\mathcal{L}}_0 = \sum_{\sigma=\uparrow,\downarrow} \tilde{d}_\sigma(\tau) \left(\partial_\tau - \tilde{\epsilon}_{d,\sigma} + i\tilde{\Delta}_\sigma \right) d_\sigma(\tau), \quad (2)$$

$$\tilde{\mathcal{L}}_{ct} = \sum_{\sigma=\uparrow,\downarrow} \tilde{d}_\sigma(\tau) (\lambda_{2,\sigma} \partial_\tau + \lambda_{1,\sigma}) \tilde{d}_\sigma(\tau) + \lambda_3 \tilde{n}_\uparrow(\tau) \tilde{n}_\downarrow(\tau), \quad (3)$$

$$\tilde{\mathcal{L}}_U = \tilde{U} \tilde{n}_\uparrow \tilde{n}_\downarrow. \quad (4)$$

In this re-arrangement the term $\tilde{\mathcal{L}}_0$ forms the starting point for the perturbative expansion and the interaction term is taken to be $\tilde{\mathcal{L}}_U + \tilde{\mathcal{L}}_{ct}$. This term gives rise to a renormalized self-energy $\tilde{\Sigma}_\sigma(\omega)$ and two-particle-reducible four-vertex $\tilde{\Gamma}_{\uparrow\downarrow}(\omega_1, \omega_2; \omega_3, \omega_4)$. The counter-terms $\lambda = (\lambda_{1,\sigma}, \lambda_{2,\sigma}, \lambda_3)$ are then determined by imposing the renormalization conditions

$$\begin{aligned} \tilde{\Sigma}_\sigma(0) &= 0, \\ \partial_\omega \tilde{\Sigma}_\sigma(\omega)|_{\omega=0} &= 0, \\ \tilde{\Gamma}_{\uparrow\downarrow}(0, 0; 0, 0) &= \tilde{U}. \end{aligned} \quad (5)$$

The presence of the counter-terms ensures that renormalization effects that have already been absorbed in the renormalized parameters are not overcounted. The counter-terms are real numbers; this is due to the Fermi liquid property of the AIM.

In many ways, this re-organization of the Lagrangian in terms of the renormalized parameters is similar to the corresponding practice in High Energy Physics (see Ref.²⁸ for instance). The motivation is largely the same, to re-express the Lagrangian in terms of physical parameters. Nevertheless there are conspicuous differences. For instance, in our system there are natural upper and lower energy cut-offs provided by the metal's lattice spacing and sample size respectively. Therefore the technicalities of the regularization procedure, which can be rather complex for many-loop calculations, do not enter our discussion at all.

For the purposes of this article we use the NRG to determine the renormalized parameters²²; note however, that in certain cases they can be determined entirely within RPT without appealing to an external method^{26,27,29}. Given the renormalized parameters, Eq. (5) is imposed in some approximation for $\tilde{\Sigma}_\sigma(\omega)$; the counter-terms thus depend on the chosen approximation to the self-energy, whereas the renormalized parameters are independent of it, and are in a one-to-one correspondence with the bare parameters that define the model. We can relate the renormalized parameters $\tilde{\epsilon}_{d,\sigma}, \tilde{\Delta}_\sigma$ to the bare ones through

$$\begin{aligned} \tilde{\epsilon}_{d,\sigma} &= z_\sigma (\epsilon_{d,\sigma} + \Sigma_\sigma(0)), \\ \tilde{\Delta}_\sigma &= z_\sigma \Delta, \end{aligned} \quad (6)$$

where

$$z_\sigma = \frac{1}{1 - \partial_\omega \Sigma_\sigma(\omega)|_{\omega=0}}, \quad (7)$$

and similarly we relate the renormalized self-energy to the bare quantity through

$$\tilde{\Sigma}_\sigma(\omega) = z_\sigma (\Sigma_\sigma(\omega) - \omega \partial_\omega \Sigma_\sigma(\omega)|_{\omega=0} - \Sigma_\sigma(0)). \quad (8)$$

We eliminate the quantities $\partial_\omega \Sigma_\sigma(\omega)|_{\omega=0}$ and $\Sigma_\sigma(0)$ in favour of $\tilde{\epsilon}_d$ and z_σ to obtain

$$\tilde{\epsilon}_{d,\sigma} + \tilde{\Sigma}_\sigma(\omega) = z_\sigma (\Sigma_\sigma(\omega) + \epsilon_{d,\sigma}) - (1 - z_\sigma)\omega. \quad (9)$$

From Eqs. (6), (8) we find the renormalized interacting propagator

$$\tilde{G}_\sigma(\omega) = [\omega - \tilde{\epsilon}_{d,\sigma} + i\tilde{\Delta}_\sigma - \tilde{\Sigma}_\sigma(\omega)]^{-1} = z_\sigma^{-1} G_\sigma(\omega) \quad (10)$$

and thus deduce via a Fourier transform and the definition of the Green's function $G_\sigma(\tau) = \langle \tilde{d}_\sigma(\tau) \tilde{d}_\sigma(0) \rangle$ that $\tilde{d}_\sigma(\tau) = z_\sigma^{1/2} d_\sigma(\tau)$ and $\tilde{\bar{d}}_\sigma(\tau) = z_\sigma^{1/2} \bar{d}_\sigma(\tau)$.

III. AUTOMATED RPT EXPANSIONS

In this section we will describe the automation of the calculation of the self-energy. For the purposes of our calculation we will use the $T = 0$ formalism. The renormalized Green's function which will form the basis of the diagrammatic expansion is

$$\tilde{G}_\sigma^{[0]}(\omega) = \frac{1}{\omega - \tilde{\epsilon}_{d,\sigma} + i\tilde{\Delta}_\sigma \text{sign}(\omega)}. \quad (11)$$

The $T = 0$ formalism has the advantage of working directly on the real axis, thus avoiding the need for an analytic continuation, which is often fraught with its own numerical difficulties. More generally, for $m \geq 1$ we introduce the propagator

$$\tilde{G}_\sigma^{[m]}(\omega) = \tilde{G}_\sigma^{[0]}(\omega) \tilde{\Sigma}_\sigma^{[m]}(\omega) \tilde{G}_\sigma^{[0]}(\omega), \quad (12)$$

where $\tilde{\Sigma}_\sigma^{[m]}(\omega)$ denotes the \tilde{U}^m (strictly) term of the renormalized self-energy. To simplify the discussion we assume a zero magnetic field, so $\tilde{\epsilon}_{d,\sigma}$ and $\tilde{\Delta}_\sigma$ are spin-independent quantities.

Our diagrammatic approach is based on the skeleton formalism. This has the advantage of avoiding explicit reference to the counter-terms λ_1 and λ_2 . Furthermore, we introduce an effective interaction constant $\tilde{U}_e = \tilde{U} + \lambda_3$ that combines the λ_3 counter-term with the renormalized interaction constant. This allows us to tentatively carry out the expansion of $\Sigma(\omega)$ in powers of \tilde{U}_e , without having to explicitly account for λ_3 . Ultimately, our goal is to organize the calculation in powers of \tilde{U} , rather than \tilde{U}_e . This will be discussed at the end of this section, but we note for now that it requires knowledge of $\tilde{\Gamma}_{\sigma,-\sigma}(0,0;0,0)$ order-by-order in \tilde{U}_e , up to \tilde{U}_e^4 inclusive. We thus aim to generate and calculate diagrams for the self-energy and the four-vertex.



FIG. 1: The first-order correction to the renormalized self-energy. The internal line corresponds to the free quasi-particle propagator of Eq. (11) and the broken line denotes the effective interaction vertex \tilde{U}_e .

A. Generating the diagrams

Consider the first-order term given by the loop diagram of Fig. 1 and a tree-level counter-term. Since the loop is frequency independent, we see, upon imposing Eq. (5), that the first-order self-energy is $\tilde{\Sigma}_\sigma^{[1]}(\omega) = 0$. Since $\tilde{\Gamma}_{\uparrow,\downarrow}(0,0;0,0)$ is by definition equal to \tilde{U} , we find that $\lambda_3 = \mathcal{O}(\tilde{U}^2)$. Note that the cancellation of the loop to this order implies that *any* diagram with a loop will cancel with the corresponding diagram that has a counter-term in place of the loop, *to all orders* in \tilde{U} . For similar reasons we can ignore diagrams whose external legs attach to the same interaction vertex, for these do not depend on the external frequency and will cancel with the counter-term. In this sense, calculations in the renormalized theory thus involve fewer diagrams than the bare theory.

To calculate the self-energy as a power series in \tilde{U} we have, in principle, to explicitly include the six interaction vertices — five from the possibly spin-dependent counter-terms and the sixth being \tilde{U} — order-by-order in the renormalized expansion. Fortunately, in the absence of a magnetic field, explicit reference to the counter-term vertices can be avoided by setting up the perturbation theory in the skeleton formalism. We define a *skeleton diagram* as a diagram that does not contain self-energy insertions. A skeleton diagram involving n interaction vertices will necessarily contain $2n - 1$ internal lines. By replacing all of them with $\tilde{G}^{[0]}$ we construct a self-energy diagram of order n ; by replacing any $2n - 2$ lines with $\tilde{G}^{[0]}$ and the remaining line with $\tilde{G}^{[1]}$ we obtain one of the diagrams that contribute to $\tilde{\Sigma}^{[n+1]}$, and so forth. An advantage of the skeleton formalism is that it minimizes the number of diagrams that have to be accounted for, since most of the diagrams of order n can be generated from a lower-order skeleton diagram. Note that for $n < 6$ we do not need to consider diagrams with more than one insertion, since a second-order diagram with two second-order insertions would contribute a \tilde{U}^6 term.

Rather than attempt to enumerate all relevant diagrams manually, which is tedious and error prone, we used the IGRAPH library³⁰ to first construct all possible diagrams and then retain only those relevant to our calculation. Since we are only interested in relatively small orders n — the bottleneck is the numerical integration, not the diagram generation — we found it sufficient to gener-

V	$\tilde{\Sigma}$	$\tilde{\Gamma}$
2	1	2
3	2	9
4	12	58
5	73	438

TABLE I: Number of dynamic skeleton self-energy and four-vertex diagrams as a function of the number of vertices V .

ate diagrams by simply exhaustively considering all possible combinations of connecting n vertices such that no internal line begins and ends on the same vertex. By regarding each Feynman diagram as a directed graph with multiple edges, and calculating the graph's edge connectivity, we can identify and discard one-particle reducible diagrams.

In graph-theoretic terms a skeleton graph can be defined as a graph that does not contain a subgraph isomorphic to a lower-order skeleton graph. Consequently, to identify the skeleton graphs of order n we must generate and store all diagrams of order³¹ $2, 3, \dots, n-2$. To identify the non-skeleton diagrams we then bijectively map each (multi-edged) Feynman graph to a simple graph with weights encoding the spins of the multiple edges and apply the VF2 algorithm^{32,33} for the subgraph isomorphism problem to the simple graphs (this 'edge coloring' technique is necessary to apply the algorithm to multi-edge graphs). Working order-by-order we can thus generate all the skeleton diagrams up to our desired order.

The diagrams that contribute to the two-particle-reducible four-vertex can be generated in a similar way. Whereas in the case of the self-energy we only had to consider the possibility that two external legs attach to different interaction vertices, the diagrams of the four-vertex admit more complex topologies which have to be taken into account individually. The calculation is otherwise identical, except for the fact that there are only $2n-2$ internal lines corresponding to a diagram of order n . Our method can similarly be extended to higher correlation functions, but this is beyond the scope of this paper. In Table I we report the number of relevant diagrams to fifth order in \tilde{U}_e .

B. Evaluating the diagrams

Having generated all relevant self-energy diagrams we proceed to impose frequency conservation at each vertex. An n 'th order diagram for the self-energy will have $2n-1$ internal lines. These are subject to n constraints, though due to global frequency conservation only $n-1$ are independent. We thus have $2n-1-(n-1)=n$ independent frequencies, each of which corresponds to an integration variable. We thus arrive at a linear, underdetermined, system of dependent equations, $\mathbf{c}\boldsymbol{\omega} = \boldsymbol{\Omega}$, where \mathbf{c} is an $n \times (2n-1)$ matrix encoding the constraints in the form

$\sum(\text{in}) - \sum(\text{out})$, $\boldsymbol{\omega}$ a vector with $2n-1$ components, each corresponding to the frequency of an internal line, and $\boldsymbol{\Omega}$ the n -dimensional vector $(-\Omega, 0, 0, \dots, \Omega)$, where Ω is the external frequency³⁴. This can now be readily inverted to give the internal line frequencies as a function of the n integration variables $\boldsymbol{\epsilon}$ and a particular solution $\boldsymbol{\Omega}_p$ to the system³⁵

$$\boldsymbol{\omega} = \mathbf{f}\boldsymbol{\epsilon} + \boldsymbol{\Omega}^{(p)}. \quad (13)$$

This can be accomplished in a number of ways; we found it best to determine the null space using the Lenstra-Lenstra-Lovász lattice basis reduction algorithm³⁶, as this results in \mathbf{f} -matrices similar to what one would obtain by manually imposing frequency conservation (i.e. matrices whose entries are ± 1 or 0). The diagrams for the four-vertex are treated similarly: an n 'th order diagram will involve $n-1$ integration variables, resulting in an $n \times (2n-2)$ \mathbf{c} -matrix and a $(2n-2) \times (n-1)$ \mathbf{f} -matrix.

It is possible, though very inefficient, to apply the Feynman rules at this point and proceed with the numerical integration. In calculations by hand, however, it is common to analytically factorize out any particle-hole or particle-particle pair-propagators. This has the advantage of reducing the dimension of the numerical integration and consequently reducing the number of integrand evaluations needed to achieve a given precision. We can generalize this to accommodate the more general scenario of k (quasi-)particle/hole lines and define

$$\tilde{\Pi}_{\sigma;\mathbf{s}}^{(k)}(\omega_1, \dots, \omega_k) = i^k \int_{-\infty}^{\infty} d\omega' \prod_{i=1}^k G_{\sigma_i}^{[0]}(s_i \omega' + \omega_i), \quad (14)$$

where $s_i = 1$ for particle lines and $s_i = -1$ for hole lines. Due to the simple form of the propagator, the integral can be calculated analytically; the details of the calculation have been relegated to the Appendix.

Having defined the k -particle/hole propagator we will now describe an algorithm to identify instances of it from the information encoded in the \mathbf{f} -matrix. Our strategy will be to first inspect the \mathbf{f} -matrix and identify groups of Green's functions that can be combined to form a product of the form of Eq. (14). We accomplish this by traversing the \mathbf{f} -matrix column-by-column — since each column corresponds to an integration variable — and examining each column's non-zero entries. Our goal is ultimately to delete from the \mathbf{f} -matrix the columns which correspond to integration variables that have been absorbed in $\tilde{\Pi}_{\sigma;\mathbf{s}}^{(k)}$, and to delete the rows that correspond to Green's functions that comprise $\tilde{\Pi}_{\sigma;\mathbf{s}}^{(k)}$. To avoid modifying the \mathbf{f} -matrix while we are traversing it we will maintain a list L_c of columns and a list L_r of rows which are to be removed, both of which are empty at the start of the search, and we will only delete the rows and columns after all possible simplifications have been identified. We will refer to the resultant simplified matrix as the \mathbf{g} -matrix, to distinguish it from the original \mathbf{f} -matrix.

To identify instances of $\tilde{\Pi}_{\sigma;\mathbf{s}}^{(k)}$ we scan each column m of the \mathbf{f} -matrix and identify the columns with exactly

k non-zero entries μ_1, \dots, μ_k on the rows r_1, \dots, r_k ³⁷. If $m \notin L_c$ and $r_1, \dots, r_k \notin L_r$ then column m indeed corresponds to a k -particle/hole propagator; if not, and either $m \in L_c$ or at least one of $r_1, \dots, r_k \in L_r$, it means that the corresponding Green's function has already been absorbed into another propagator, and we proceed to the next column. With the j 'th k -particle/hole propagator³⁸ we will associate a matrix \mathbf{q}_j , which encodes its dependence on the remaining integration variables, and vectors σ_j , \mathbf{s}_j describing the spin and sign configuration respectively. The k frequency arguments of $\tilde{\Pi}_{\sigma_j; \mathbf{s}_j}^{(k_j)}$ will therefore be given by the rows of \mathbf{q}_j . Furthermore, we construct a k -dimensional vector $\Omega_{\mathbf{q}}$ that contains the external frequency dependence of the rows r_1, \dots, r_k , i.e. $\Omega_{\mathbf{q}} = (\Omega_{r_1}^{(p)}, \dots, \Omega_{r_k}^{(p)})$. In other words, the ω_i that appear in Eq. (14) can be obtained from the i 'th component of

$$\mathbf{q}\epsilon' + \Omega_{\mathbf{q}}, \quad (15)$$

where ϵ' denotes the free variables that remain after all propagator simplifications. After constructing the \mathbf{q} -matrix we add m to L_c and all of r_1, \dots, r_k to L_r and examine the next column. When the columns of the matrix have been exhausted we delete all columns in L_c and rows in L_r from the original \mathbf{f} -matrix, to obtain its final form \mathbf{g} . Furthermore, to account for the fact that components of the original $\Omega^{(p)}$ have been absorbed into the various $\Omega_{\mathbf{q}}$ we delete all the rows in L_r from $\Omega^{(p)}$ to obtain its final form, which we denote $\Omega^{(g)}$. Finally, we eliminate the columns in L_c from the provisional \mathbf{q} matrices.

For each diagram we thus arrive at an expression for the amplitude of the form

$$I_{\mathcal{D}} = P_{\mathcal{D}} \int d\epsilon \tilde{G}_{\sigma_1}^{[l_1]} \tilde{G}_{\sigma_2}^{[l_2]} \dots \tilde{\Pi}_{\sigma_1; \mathbf{s}_1}^{(k_1)} \tilde{\Pi}_{\sigma_2; \mathbf{s}_2}^{(k_2)} \dots, \quad (16)$$

where $P_{\mathcal{D}}$ is a complex prefactor containing powers of \tilde{U}_e , i and 2π . In Eq. (16) it is understood that the argument of $\tilde{G}_{\sigma_i}^{[l_i]}$ corresponds to the i 'th row of

$$\omega = \mathbf{g}\epsilon + \Omega^{(g)}, \quad (17)$$

which is similar to Eq. (13) but involves \mathbf{g} , the simplified form of the \mathbf{f} -matrix, and that the (vector) argument of the j 'th $\tilde{\Pi}_{\sigma_j; \mathbf{s}_j}^{(k_j)}$ is given by Eq. (15), with the corresponding \mathbf{q}_j and $\Omega_{\mathbf{q}_j}$. We remark that while the final integral of Eq. (16) is at least one-dimensional for all self-energy diagrams, some four-vertex diagrams factorize completely.

To illustrate this with an example consider the diagram of Fig. 2. We find that the amplitude is proportional to

$$\int d\epsilon \tilde{G}_{\sigma}^{[0]}(\epsilon_1 - \epsilon_3 + \Omega) \tilde{G}_{\sigma}^{[0]}(\epsilon_2 - \epsilon_3 + \Omega) \times \tilde{G}_{-\sigma}^{[0]}(\epsilon_1) \tilde{G}_{-\sigma}^{[0]}(\epsilon_2) \tilde{G}_{-\sigma}^{[0]}(\epsilon_3), \quad (18)$$

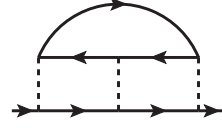


FIG. 2: One of the two diagrams that contribute to the self-energy to third order in \tilde{U}_e .

or in matrix notation,

$$\mathbf{f} = \begin{bmatrix} 1 & 0 & -1 \\ 0 & 1 & -1 \\ 1 & 0 & 0 \\ 0 & 1 & 0 \\ 0 & 0 & 1 \end{bmatrix}, \quad \Omega^{(p)} = \begin{bmatrix} \Omega \\ \Omega \\ 0 \\ 0 \\ 0 \end{bmatrix}. \quad (19)$$

We begin with the first column and identify the first particle-particle pair propagator by the first and third row entries. The propagator is $\tilde{\Pi}_{\sigma, \mathbf{s}}^{(2)}$, where $\sigma = (\sigma, -\sigma)$, because the first and third Green's functions have spin σ and $-\sigma$ respectively, and $\mathbf{s} = (1, 1)$ because $\mathbf{f}_{11} = \mathbf{f}_{31} = 1$. Having 'used' the Green's functions in question, we mask their corresponding entries in \mathbf{f} by appending '1' to L_c and '1,3' to L_r so that $L_c = \{1\}$ and $L_r = \{1, 3\}$. We temporarily associate this propagator with the matrices

$$\mathbf{q}_1 = \begin{bmatrix} 1 & 0 & -1 \\ 1 & 0 & 0 \end{bmatrix}, \quad \Omega_{\mathbf{q}_1} = \begin{bmatrix} \Omega \\ 0 \end{bmatrix}, \quad (20)$$

constructed from the first and third rows of \mathbf{f} and $\Omega^{(p)}$ in Eq. (19). We now examine the second column of \mathbf{f} in Eq. (19) and note that the two non-zero entries are contained in the second and fourth rows, neither of which is in L_r . This is thus another instance of $\Pi_{(\sigma, -\sigma); (1, 1)}^{(2)}$, and after updating $L_c = \{1, 2\}$, and $L_r = \{1, 3, 2, 4\}$. We associate this propagator with a \mathbf{q}_2 matrix equal to Eq. (20). We proceed to the third column and examine the possibility that it corresponds to a triple propagator. We conclude that it does not, since its non-zero elements appear on rows 1, 2, 5, the first two of which are already in L_r . Having exhausted the columns of \mathbf{f} , the final step is to remove all columns in L_c and all rows in L_r from \mathbf{f} to obtain \mathbf{g} , and all column in L_c from \mathbf{q}_1 , \mathbf{q}_2 to obtain their final simplified form and remove the references to the variables of integration that have been eliminated. To conclude the procedure we also delete all rows in L_r from $\Omega^{(p)}$, to obtain $\Omega^{(g)}$. We thus have $\mathbf{f} = [1]$, $\Omega^{(g)} = [0]$ and

$$\mathbf{q}_1 = \mathbf{q}_2 = \begin{bmatrix} 1 \\ 0 \end{bmatrix}, \quad \Omega_{\mathbf{q}_2} = \Omega_{\mathbf{q}_1} = \begin{bmatrix} \Omega \\ 0 \end{bmatrix}, \quad (21)$$

and the amplitude in Eq. (18) simplifies to

$$\int d\epsilon_1 \tilde{G}_{\sigma}^{[0]}(\epsilon_1) \left[\Pi_{(\sigma, -\sigma); (1, 1)}^{(2)}(\epsilon_1 + \Omega, 0) \right]^2. \quad (22)$$

The final step in our calculation is the numerical integration, which is handled with adaptive quadrature³⁹ and cubature methods⁴⁰. By evaluating *vectors* of points at every iteration, the calculation can be seamlessly parallelized to take advantage of modern computer architectures. Note that it is possible, especially in the absence of a magnetic field, for two distinct diagrams to be equal numerically. We test for this by evaluating each diagram individually at a randomly chosen frequency of order $\tilde{\Delta}$, and, if an equal pair is found, ensuring that only one of the diagrams is included in the integration, with an adjusted prefactor, is included in the integration. A similar situation occurs in the case of particle-hole symmetry, where $\tilde{\epsilon}_d = 0$, rendering $\tilde{G}^{[0]}(\omega)$ an odd function of frequency and leading to the numerical cancellation of several diagrams.

C. Assembling the RPT

So far we have been working order-by-order in the effective interaction $\tilde{U}_e = \tilde{U} + \lambda_3$, expressing the self-energy as

$$\tilde{\Sigma}(\omega) = \sum_{n=2}^{\infty} \gamma_n(\omega) \tilde{U}_e^n. \quad (23)$$

Ultimately, we aim to obtain $\tilde{\Sigma}(\omega)$ as a power series in \tilde{U} rather than \tilde{U}_e . To accomplish this, we note that the counter-term λ_3 is defined as in Eq. (5). By calculating the renormalized four-vertex at zero frequency we can thus obtain \tilde{U} as a power series in \tilde{U}_e ,

$$\tilde{U} = \tilde{\Gamma}_{\uparrow\downarrow}(0, 0; 0, 0) = \tilde{U}_e + \sum_{n=2}^{\infty} \alpha_n \tilde{U}_e^n. \quad (24)$$

Working order-by-order we can invert this equation:

$$\tilde{U}_e = \tilde{U} + \sum_{n=2}^{\infty} \beta_n \tilde{U}^n, \quad (25)$$

where

$$\begin{aligned} \beta_2 &= -\alpha_2, \\ \beta_3 &= 2\alpha_2^2 - \alpha_3, \\ \beta_4 &= -5\alpha_2^3 + 5\alpha_2\alpha_3 - \alpha_4, \\ \beta_5 &= 14\alpha_2^4 - 21\alpha_2^2\alpha_3 + 6\alpha_2\alpha_4 + 3\alpha_3^2 - \alpha_5. \end{aligned} \quad (26)$$

Thus, the calculation of the self-energy in terms of \tilde{U}_e can be rewritten as a series in \tilde{U}

$$\tilde{\Sigma}(\omega) = \sum_{n=2}^{\infty} \delta_n(\omega) \tilde{U}^n, \quad (27)$$

where

$$\begin{aligned} \delta_2 &= \gamma_2(\omega), \\ \delta_3 &= -2\alpha_2\gamma_2(\omega) + \gamma_3(\omega), \\ \delta_4 &= (5\alpha_2^2 - 2\alpha_3)\gamma_2(\omega) - 3\alpha_2\gamma_3(\omega) + \gamma_4(\omega), \\ \delta_5 &= (-14\alpha_2^3 + 12\alpha_3\alpha_2 - 2\alpha_4)\gamma_2(\omega) \\ &\quad + (9\alpha_2^2 - 3\alpha_3)\gamma_3(\omega) - 4\alpha_2\gamma_4(\omega) + \gamma_5(\omega). \end{aligned} \quad (28)$$

These relations enable us to deduce the renormalized expansion from the bare one and show explicitly how the inclusion of counter-terms results in the re-organization of the series.

D. Checks

To check our calculation for the self-energy we can relate the RPT to the perturbation theory of Yamada and Yosida²⁻⁴ by replacing \tilde{U}_e in Eq. (23) with the bare U , the parameters $\tilde{\epsilon}_d, \tilde{\Delta}$ with their bare counter-parts and setting all the counter-terms equal to zero. Similarly, we can check the four-vertex against the calculation of Ref.²¹. We find that the analytic results

$$\begin{aligned} \partial_\omega \Sigma(0) &= -\left(3 - \frac{\pi^2}{4}\right)u^2 - \left(105 - \frac{45\pi^2}{4} + \frac{\pi^4}{16}\right)u^4 + \dots \\ \Gamma_{\uparrow\downarrow}(0, 0; 0, 0) &= U \left[1 + \left(15 - \frac{3\pi^2}{2}\right)u^2 + \dots\right], \end{aligned} \quad (29)$$

where $u = U/\pi\Delta$, are reproduced by our calculation.

IV. RESULTS

In this section we present numerical results for the irreducible self-energy and resultant spectral density. For all the calculations we fix $\pi\Delta = D/100$, where D is the conduction band width, and $U = 3\pi\Delta$. In our discussion we consider the following parameter configurations: (i) a symmetric model with $\epsilon_d = -U/2$; (ii) a model with weak asymmetry $\epsilon_d = -1.2\pi\Delta$; and (iii) a model with pronounced asymmetry and $\epsilon_d = -3\pi\Delta$. In all cases, the scale of the problem is set by the renormalized density of states at the Fermi level,

$$\tilde{\rho}_0 = \frac{\tilde{\Delta}/\pi}{\tilde{\epsilon}_d^2 + \tilde{\Delta}^2}. \quad (30)$$

We use $\tilde{\rho}_0$ to define the Kondo temperature T_K as $T_K = 1/4\tilde{\rho}_0$; in the Kondo limit this reduces to the usual definition of T_K in terms of the susceptibility²¹. We will

A. Self-energy

For comparison purposes we will juxtapose the renormalized self-energy obtained from RPT with the corresponding result obtained from the NRG. Since NRG calculations are set up with the bare self-energy in mind, we

have to use Eq. (9) to relate the two quantities. For the imaginary part we find that

$$\text{Im}\tilde{\Sigma}_\sigma(\omega) = z_\sigma \text{Im}\Sigma_\sigma(\omega). \quad (31)$$

We remark that inaccuracies in our NRG calculation result in a slightly non-zero $\text{Im}\tilde{\Sigma}_\sigma(0)$; to correct for this we offset our results by a small imaginary number. An equation similar to Eq. (31) can be derived for the real part; in practice however, it is of limited use. The reason is that the renormalized parameters are not determined from the NRG using the definitions in Eq. (6) but from the effective linear chain Hamiltonian (for more information see the Appendix of Ref.²²). Since the low-energy limit of the real part of Eq. (9) relies crucially on the numerical cancellation between $\Sigma(\omega)$ and $(z-1)\omega$, we found it difficult to obtain a result for $\text{Re}\tilde{\Sigma}(\omega)$ with a vanishing derivative at zero frequency. It is for this reason that we only show NRG results for $\text{Im}\tilde{\Sigma}(\omega)$. Note that due to the NRG's successive elimination of higher energy scales we expect that its estimate for $\tilde{\Sigma}(\omega)$ will only be accurate in the low frequency sector.

We begin by discussing the symmetric model (case (i)). As we have already remarked, in the presence of particle-hole symmetry $\tilde{\epsilon}_d = 0$ and the propagator is an odd function of frequency. The parity of the Green's function also results in the cancellation of the particle-hole and particle-particle propagators

$$\tilde{\Pi}_{\sigma;(1,1)}^{(2)}(\omega_1, \omega_2) = -\tilde{\Pi}_{\sigma;(1,-1)}^{(2)}(\omega_1, \omega_2), \quad (32)$$

and consequently the odd-order terms of the self-energy vanish for all frequencies. Using the method described in Ref.²² we find that $\tilde{\Delta} = 2.54 \times 10^{-4}$ and $\tilde{U} = 7.95 \times 10^{-4}$, giving $\tilde{U}/\pi\tilde{\Delta} = 0.994$. That this ratio is almost 1 is no coincidence; in the Kondo limit a universal scale, the Kondo temperature T_K emerges and $\tilde{U} \rightarrow 4T_K, \pi\tilde{\Delta} \rightarrow 4T_K$ ¹⁹.

In all cases, the RPT estimate of the renormalized self-energy will always be exact in the limit $\omega \rightarrow 0$, in the sense of Eq. (5). At particle-hole symmetry, and for small but finite frequencies $|\omega\tilde{\rho}_0| \ll 1$, the ω^2 coefficient of $\tilde{\Sigma}(\omega)$ is reproduced exactly¹⁹ by the second-order calculation; the fourth order term does not contribute terms of order ω^2 . As we increase $|\omega|$ the dominant term is the ω^4 term, which is not exactly given by the second-order calculation; this is corrected by the fourth-order contribution, extending the domain of validity of the RPT. At higher frequencies the disparity between the two RPT curves suggests the breakdown of the expansion; to obtain reliable results one must calculate the higher-order terms. We thus expect more elaborate approximations within RPT to continually extend the domain of validity of the resultant $\tilde{\Sigma}(\omega)$. Were we to have, somehow, the ability to take into account *all* Feynman diagrams to all orders we would recover a $\tilde{\Sigma}(\omega)$ exact for all frequencies, though clearly then we would also be able to calculate $\Sigma(\omega)$ in the first place.

Next, we discuss a slightly asymmetric model with $\epsilon_d = -1.2\pi\Delta$, for which we find that $\tilde{\epsilon}_d = 2.14 \times 10^{-5}$, $\tilde{\Delta} = 2.93 \times 10^{-4}$ and $\tilde{U} = 9.18 \times 10^{-4}$. The non-zero but small in magnitude $\tilde{\epsilon}_d$ now gives rise to odd-order terms in $\tilde{\Sigma}(\omega)$. From Fig. (4) we see that the third and fifth order terms are small in value and essentially only slightly modify the second and fourth order curves respectively. To determine the stability of the series to order n we see that to simply look at the $n+1$ term is not sufficient, since the $n+2$ terms can still remain important.

Finally, we turn our attention to Fig. (5) and case (iii), a very asymmetric model with $\epsilon_d = -3\pi\Delta$. For small $|\omega|$ we find again that the RPT is in good agreement with the NRG and that the lower order contributions dominate the result. A dramatic breakdown of the expansion, in both the real and imaginary components, is evident for small negative value of ω in contrast to cases (i) and (ii) where it is reasonably well-behaved even around $\omega\tilde{\rho}_0 \approx 0.5$.

B. Spectral densities

We define the interacting Green's function

$$\tilde{G}_\sigma(\omega) = \frac{1}{\omega - \tilde{\epsilon}_d + i\tilde{\Delta} - \tilde{\Sigma}^R(\omega)}, \quad (33)$$

where $\tilde{\Sigma}^R(\omega)$ is the *retarded* self-energy, which, as usual, differs from the causal $\tilde{\Sigma}(\omega)$ one obtains from the diagrammatics only by a $\text{sign}(\omega)$ term in the imaginary part. We now turn our attention to the quasi-particle spectral density, defined as $\tilde{\rho}(\omega) = -\frac{1}{\pi}\text{Im}\tilde{G}(\omega)$ and express it in terms of the renormalized parameters as

$$\tilde{\rho}(\omega) = \frac{1}{\pi} \frac{\tilde{\Delta} - \text{Im}\tilde{\Sigma}^R(\omega)}{(\omega - \tilde{\epsilon}_d - \text{Re}\tilde{\Sigma}^R(\omega))^2 + (\tilde{\Delta} - \text{Im}\tilde{\Sigma}^R(\omega))^2}. \quad (34)$$

Note that the spectral density is sensitive to the *reducible* self-energy. The low-frequency properties of the n 'th order spectral density are thus the result of competition between higher-order irreducible self-energies and powers of $\tilde{G}^{[0]}(\omega)$ combined with powers of lower-order irreducible self-energies.

Results for cases (i), (ii) and (iii) are shown in Figs. 6, 7 and 8 respectively. To avoid the instability in the real part of $\tilde{\Sigma}(\omega)$ we do not use Eq. (34) directly to extract the result from the NRG; instead we use the NRG result for $\rho(\omega)$ and, from Eq. (10), $\tilde{\rho}(\omega) = \rho(\omega)/z$. Note that $\tilde{\rho}_0$ is calculated from the renormalised parameters, and consequently, due to inaccuracies in our NRG calculation, the ratio $\rho(\omega=0)/\tilde{\rho}_0$ may differ from 1.

For the particle-hole symmetric model of case (i) we find again that the second and fourth order terms coincide for small ω and start deviating from each other and the NRG result as $|\omega|$ is increased, with the RPT4 curve being in closer agreement with the latter. This picture persists in Fig. (7) where, as in the case of the self-energy,

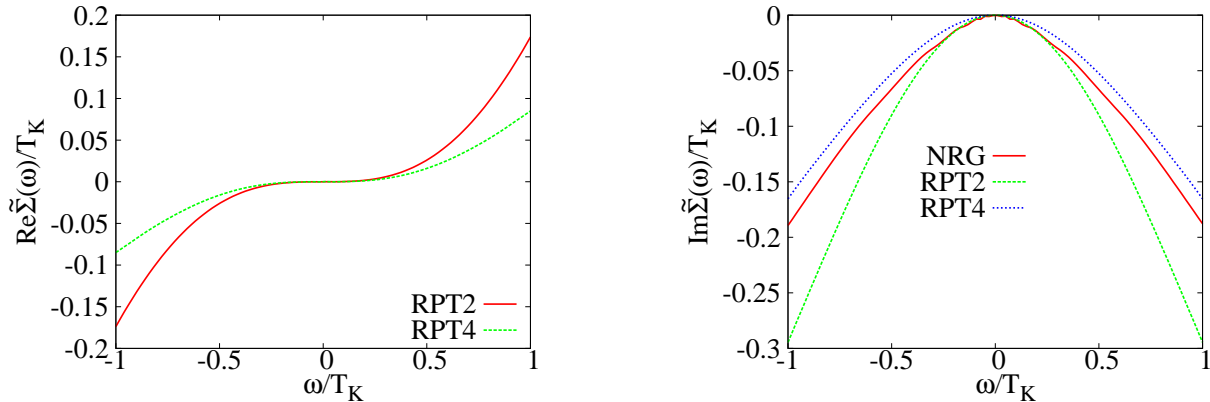


FIG. 3: The real (left) and imaginary (right) parts of the renormalized self-energy for the particle-hole symmetric model.

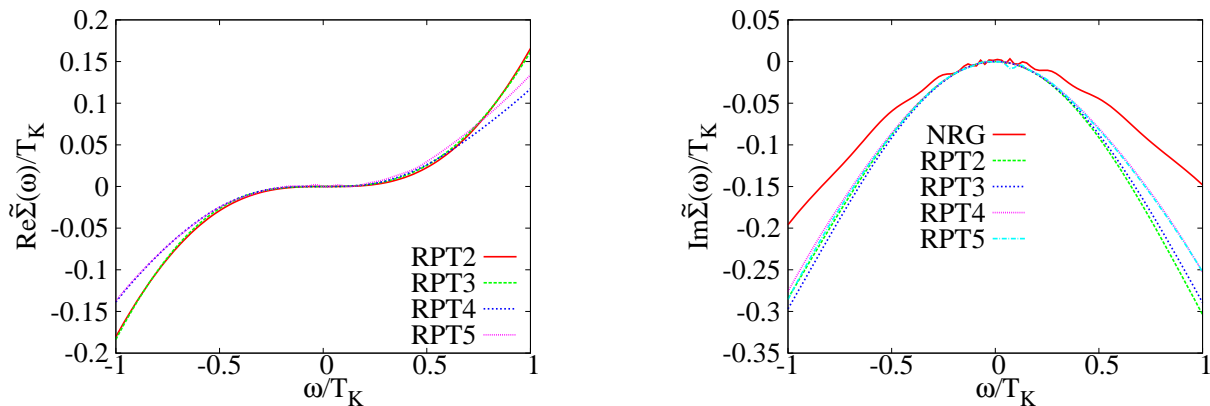


FIG. 4: The real (left) and imaginary (right) parts of the renormalized self-energy for the weakly asymmetric model (model (ii)).

two pairs of similar curves emerge. We remark that at particle-hole symmetry $\tilde{\rho}(\omega = 0) = (\pi\tilde{\Delta})^{-1}$; away from particle-hole symmetry $\tilde{\rho}(\omega = 0)$ is given exactly by the renormalized parameters as per Eq. (30).

V. CONCLUSION

In this paper we have presented a relatively simple way of automating the calculation of the renormalized self-energy so that it can be carried out by a computer without user intervention. Our presentation was logically partitioned into three steps: the diagram generation, the application of the rules and analytic simplification of the integrals and the numerical integration of the diagrams.

To illustrate the usefulness of the method we have calculated the self-energy up to fifth-order inclusive, a cal-

culation which would otherwise be extremely tedious to perform by hand. We performed the calculation for three possible values of the asymmetry and found the results to be in good agreement with the NRG in the meaningful low frequency region. In all cases we find that the higher order terms contribute more at higher frequencies, with RPT becoming increasingly more accurate as $\omega \rightarrow 0$.

Though our discussion has been confined to the single-impurity Anderson model, the method here is readily generalisable to other models by replacing the Green's function with the appropriate one. Unfortunately, the calculation of the k -particle/hole propagator of the Appendix relies on the linear dependence of $[\tilde{G}^{[0]}(\omega)]^{-1}$ on ω and thus does not generalize. This is not too serious an obstacle, for we can always numerically evaluate and tabulate the cases $k = 2, 3$ which most commonly appear. A further generalization can be realized by replacing the

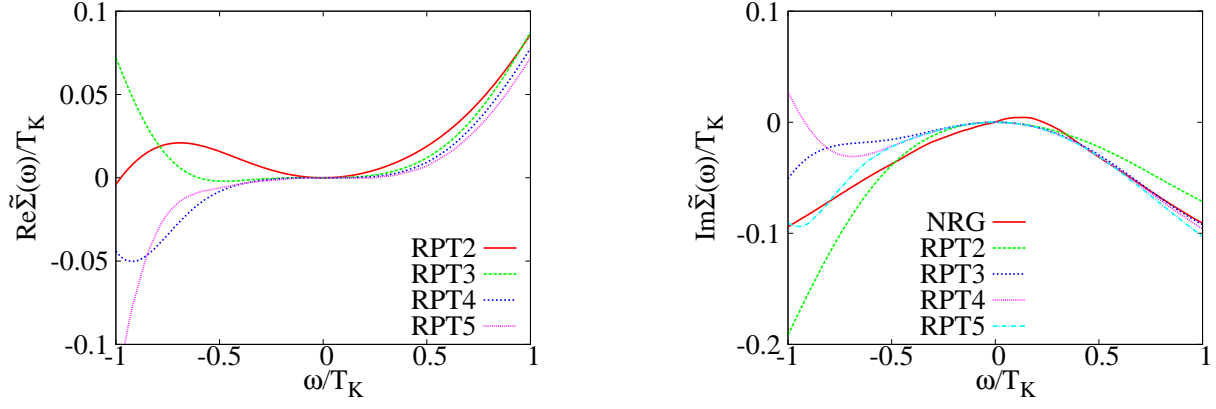


FIG. 5: The real (left) and imaginary (right) parts of the renormalized self-energy for the strongly asymmetric model (model (iii)).

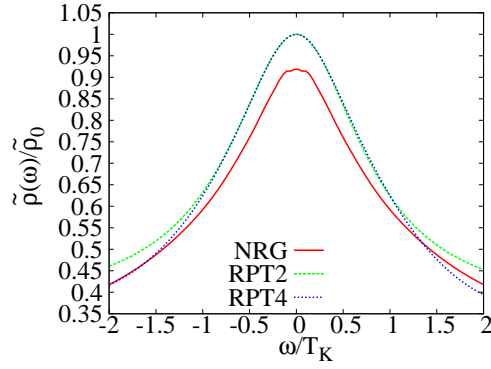


FIG. 6: The spectral density for the particle-hole symmetric model (model (i)).

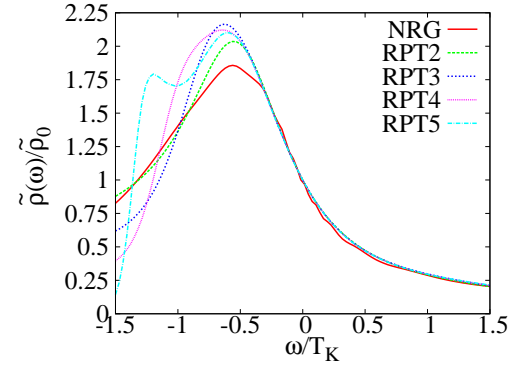


FIG. 8: The spectral density for the very asymmetric model (model (iii)).

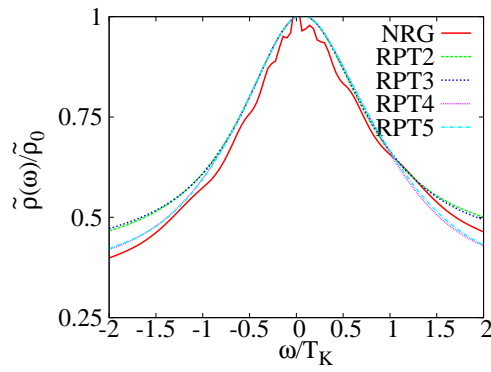


FIG. 7: The spectral density for model (ii), with some asymmetry.

scalar propagator with a matrix quantity to obtain calculate the behaviour of the impurity out of equilibrium⁴¹. This is of particular importance in the study of quantum dots under a bias voltage.

ACKNOWLEDGMENTS

V.P. would like to acknowledge the financial support of the Engineering and Physical Sciences Research Council.

Appendix: Appendix

In Eq. (14) we define a k -particle/hole propagator as

$$\tilde{\Pi}_{\sigma;\mathbf{s}}^{(k)}(\omega_1, \dots, \omega_n) = i^n \int_{-\infty}^{\infty} d\omega' \prod_{i=1}^k G_{\sigma_i}^{[0]}(s_i \omega' + \omega_i). \quad (\text{A.1})$$

where $s_i \in \{-1, 1\}$. Due to the sign term in the causal Green's function (Eq. (11)), the integrand can be thought of as a piecewise function in ω' . We begin by identifying the points y_i , which we will call *nodes*, where $s_i y_i + \omega_i = 0$. We can ensure by appropriate labelling of the nodes that $-\infty \geq y_1 \geq y_2 \dots \geq y_n$. For brevity, we write the i 'th Green's function in the form

$$\tilde{G}_{\sigma_i}^{[0]}(\omega) = \frac{s_i}{\omega - \alpha_i(\omega)}, \quad (\text{A.2})$$

where $\alpha_i = s_i [-\omega_i + \epsilon_{d,\sigma_i} - i\Delta \text{sign}(s_i \omega + \omega_i)]$. We temporarily make the assumption, which will be lifted later, that all the α_i are distinct. Written as a product of terms of the form of Eq. (A.2), the integrand depends explicitly on ω' but also implicitly through the dependence of the α . Having identified the nodes we can rewrite Eq. (A.1) as

$$i^{-n} \tilde{\Pi}_{\sigma;s}^{(n)}(\omega_1, \dots, \omega_n) = J(y_1, y_n) + \sum_{i=1}^{n-1} F(y_i, y_{i+1}), \quad (\text{A.3})$$

where

$$F(y_i, y_{i+1}) = \int_{y_i}^{y_{i+1}} d\omega' \prod_{i=1}^k G_{\sigma_i}^{[0]}(s_i \omega' + \omega_i)$$

$$J(y_1, y_n) = \lim_{\Lambda \rightarrow \infty} \left\{ \int_{-\Lambda}^{y_1} d\omega' \prod_{i=1}^k G_{\sigma_i}^{[0]}(s_i \omega' + \omega_i) \right. \quad (\text{A.4})$$

$$\left. + \int_{y_n}^{\Lambda} d\omega' \prod_{i=1}^k G_{\sigma_i}^{[0]}(s_i \omega' + \omega_i) \right\}. \quad (\text{A.5})$$

The decomposition of the real axis into intervals on which the integrand does not change form means that we can perform a partial fraction decomposition with coefficients specific to the region. Hence we can write

$$\frac{1}{(\omega' - \alpha_1)(\omega' - \alpha_2) \dots (\omega' - \alpha_n)} = \sum_{i=1}^n \frac{\beta_i}{\omega' - \alpha_i}, \quad (\text{A.6})$$

where $\beta_j = 1/f'(\alpha_j)$, $f(\omega) = (\omega - \alpha_1) \dots (\omega - \alpha_n)$. We can now simply integrate each partial fraction separately. Let $\alpha^{(i)}$ and $\beta^{(i)}$ denote the values of the relevant quantities in the region (y_i, y_{i+1}) . Then

$$F(y_i, y_{i+1}) = \sum_{j=1}^n \beta_j^{(i)} \text{Ln} \left(\frac{y_{i+1} - \alpha_j^{(i)}}{y_i - \alpha_j^{(i)}} \right)$$

$$J(y_1, y_n) = \sum_{j=1}^n \left[\beta_j^{(0)} \text{Ln} (y_1 - \alpha_j^{(0)}) - \beta_j^{(n+1)} \text{Ln} (y_n - \alpha_j^{(n+1)}) \right], \quad (\text{A.7})$$

where $\text{Ln}(z)$ denotes the principal branch of the complex logarithm defined as $\ln|z| + i \text{Arg}(z)$, $-\pi < \text{Arg}(z) < \pi$ and the labels 0, $n+1$ denote the values of the underlying quantities in the intervals $(-\infty, y_1)$ and (y_n, ∞) respectively.

In practical applications we may encounter numerical difficulties if the ω_i are such that any two α_i in a particular region coincide, or nearly coincide. This will cause our partial fraction to break down. We deal with this in a crude yet effective manner: when any α_i, α_j are too close to each other, we separate them by a very small, arbitrary constant. After separating the offending α_i, α_j it is important to update the values of the corresponding y_i, y_j to ensure the consistency of the calculation.

-
- ¹ P. W. Anderson, Phys. Rev. **124**, 41 (Oct 1961)
² K. Yosida and K. Yamada, Prog. Theor. Phys **46**, 44 (1970)
³ K. Yamada, Prog. Theor. Phys **53**, 35 (1975)
⁴ K. Yosida and K. Yamada, Prog. Theor. Phys **53**, 35 (1975)
⁵ B. Horvatić and V. Zlatić, Phys. Status Solidi B **99**, 251 (1980)
⁶ B. Horvatić and V. Zlatić, Phys. Status Solidi B **111**, 65 (1982)
⁷ N. E. Bickers, Rev. Mod. Phys. **59**, 845 (Oct 1987)
⁸ N. Andrei, K. Furuya, and J. Lowenstein, Rev. Mod. Phys. **55**, 331 (1983)
⁹ P. B. Wiegmann and A. M. Tsvelick, J. Phys. C **16**, 2281 (1983)
¹⁰ K. G. Wilson, Rev. Mod. Phys. **47**, 773 (Oct 1975)
¹¹ H. R. Krishna-murthy, J. W. Wilkins, and K. G. Wilson, Phys. Rev. B **21**, 1003 (Feb 1980)
¹² A. C. Hewson, *The Kondo problem to heavy fermions*, Cambridge studies in magnetism (Cambridge University Press, 1997)
¹³ A. Georges, G. Kotliar, W. Krauth, and M. J. Rozenberg, Rev. Mod. Phys. **68**, 13 (Jan 1996)
¹⁴ P. Nozières, J. Low Temp. Phys. **17**, 31 (1974)
¹⁵ This follows from a phase-space argument and does not imply that the interaction constant is small.
¹⁶ F. D. M. Haldane, Phys. Rev. Lett. **40**, 416 (Feb 1978)
¹⁷ E. Sela and J. Malecki, Phys. Rev. B **80**, 233103 (Dec 2009)
¹⁸ C. Mora, C. Pascu Moca, J. von Delft, and G. Zarand, ArXiv e-prints(Sep. 2014), arXiv:1409.3451
¹⁹ A. C. Hewson, Phys. Rev. Lett. **70**, 4007 (Jun 1993)
²⁰ A. C. Hewson, Adv. Phys. **43**, 543 (1994)
²¹ A. C. Hewson, J. Phys. Condens. Matter **13**, 10011 (2001)
²² A. C. Hewson, A. Oguri, and D. Meyer, Eur. Phys. J. B **40**, 177 (2004)
²³ A. C. Hewson, J. Phys. Condens. Matter **18**, 1815 (2006)
²⁴ A. C. Hewson, J. Bauer, and W. Koller, Phys. Rev. B **73**, 045117 (Jan 2006)
²⁵ J. Bauer and A. C. Hewson, Phys. Rev. B **76**, 035119 (Jul 2007)
²⁶ K. Edwards and A. C. Hewson, J. Phys. Condens. Matter **23**, 045601 (2011)

- ²⁷ K. Edwards, A. C. Hewson, and V. Pandis, Phys. Rev. B **87**, 165128 (Apr 2013)
- ²⁸ M. E. Peskin and D. V. Schroeder, *An Introduction To Quantum Field Theory (Frontiers in Physics)* (Westview Press, 1995)
- ²⁹ V. Pandis and A. C. Hewson, ArXiv e-prints(Dec. 2014), arXiv:1412.5631
- ³⁰ G. Csardi and T. Nepusz, InterJournal **Complex Systems**, 1695 (2006), <http://igraph.org>
- ³¹ Diagrams that contain insertions of order $n - 1$ can only produce a static contribution.
- ³² T. A. Junttila and P. Kaski, in *ALENEX*, Vol. 7 (2007) pp. 135–149
- ³³ L. P. Cordella, P. Foggia, C. Sansone, and M. Vento, in *3rd IAPR-TC15 Workshop on Graph-Based Representations in Pattern Recognition* (2001) pp. 149–159
- ³⁴ This form of Ω follows by adopting the convention to place the constraints emerging from frequency conservation on the vertices that attach to the incoming and outgoing legs on the first and last row of \mathbf{c} respectively.
- ³⁵ Note that the matrix \mathbf{f} is not unique but we can always perform a unitary transformation so that all its entries are equal to 0 or ± 1 .
- ³⁶ A. Lenstra, J. Lenstra, H.W., and L. Lovsz, *Mathematische Annalen* **261**, 515 (1982)
- ³⁷ Since we are using the LLL algorithm to find \mathbf{f} we also know that $|\mu_1| = \dots = |\mu_k| = 1$, since any non-zero entry will be ± 1 .
- ³⁸ The variable j here is merely a label; the first k -particle/hole propagator we identify is $j = 1$, and so on.
- ³⁹ M. Galassi, J. Davies, J. Theiler, B. Gough, G. Jungman, M. Booth, and F. Rossi, *Gnu Scientific Library: Reference Manual* (Network Theory Ltd., 2003)
- ⁴⁰ S. G. Johnson, “cubature,” <http://ab-initio.mit.edu/wiki/index.php/Cubature> (2008), [Online; accessed 19-July-2008]
- ⁴¹ A. Oguri, Phys. Rev. B **64**, 153305 (Sep 2001)